

Central Cluster Galaxies: A Hotspot for Detectable Gravitational Waves from Black Hole Mergers

YIHAO ZHOU ¹, TIZIANA DI MATTEO,¹ NIANYI CHEN,^{2,1} LUKE ZOLTAN KELLEY,³ LAURA BLECHA,⁴ YUEYING NI,⁵ SIMEON BIRD,⁶
YANHUI YANG,⁶ AND RUPERT CROFT¹

¹*McWilliams Center for Cosmology, Department of Physics, Carnegie Mellon University, Pittsburgh, PA 15213, USA*

²*School of Natural Sciences, Institute for Advanced Study, Princeton, NJ 08540, USA*

³*Department of Astronomy, University of California, Berkeley, Berkeley, CA 94720, USA*

⁴*Physics Department, University of Florida, Gainesville, FL 32611, USA*

⁵*Center for Astrophysics | Harvard & Smithsonian, Cambridge, MA 02138, US*

⁶*Department of Physics & Astronomy, University of California, Riverside, 900 University Ave., Riverside, CA 92521, USA*

ABSTRACT

We model continuous gravitational wave (CW) sources detectable by pulsar timing arrays (PTAs), using the ASTRID cosmological simulation. The most detectable single sources are in the low-frequency bins and are produced by the most supermassive black hole (SMBH) mergers (with $M_{\text{BH}} \sim 10^{10-11} M_{\odot}$ in the most massive galaxies $M_* \sim 10^{12} M_{\odot}$). Remarkably, these mergers (mostly at $z < 0.3$) occur within massive galaxies residing at the center of galaxy clusters. Particularly striking in ASTRID is a triple merger event, where two subsequent mergers in the same cluster core generate high-detection-probability CW signals at $\sim 2\text{nHz}$ and $\sim 10\text{nHz}$. We expect electromagnetic signatures from these events: either single or dual active galactic nuclei (AGN) and massive host galaxies that are undergoing significant star formation. We establish a novel connection between these high-mass, central cluster mergers, occurring in galaxies with active star formation and AGN, and the formation process of the central cluster galaxy in ASTRID. This provides new insights into the low-frequency gravitational wave sky and informs future multi-messenger searches for PTA CW sources.

1. INTRODUCTION

Massive black holes (MBHs) at the heart of massive galaxies are predicted to form binaries as a result of galaxy merging. Two MBHs sink to the center of a galaxy merger via dynamical friction, and then their orbit continues to decay, reaching $\sim 10^{-2}$ pc scales through a combination of stellar scattering and circumbinary disk torques. Below these scales, MBH binary hardening is dominated by the emission of gravitational waves (GWs). Such GW signals are the main target for Pulsar Timing Arrays (PTAs) and the Laser Interferometer Space Antenna (LISA), which both open a new window other than traditional electromagnetic (EM) information to understand the population of MBHs.

Multiple PTA collaborations have recently reported the first detection of GWs in the nanohertz frequency band (NANOGrav (Agazie et al. 2023a); CPTA (Xu et al. 2023); PPTA (Reardon et al. 2023); EPTA+InPTA (EPTA Collaboration et al. 2023)). Despite their different modeling choices, their results are consistent with each other, agreeing within 1σ (Agazie et al. 2024).

Many predictions of the gravitational-wave background (GWB) produced by inspiralling MBHs have been made (e.g., Sesana et al. (2008); Ravi et al. (2012); Kelley et al. (2017); Izquierdo-Villalba et al. (2022); also see Table.2 in Kelley et al. (2017)). However, all predict a GWB amplitude smaller

than that measured observationally. Sato-Polito et al. (2024) and Sato-Polito & Zaldarriaga (2024) demonstrated that even with the optimal scenario for the MBH merging history and accretion, the difference between predictions and observations is still significant, and the current GW measurement requires roughly ~ 10 times more black holes than suggested by local observation.

Continuous waves (CWs) from individual MBH binaries are expected to be observed in the next few years (Rosado et al. 2015; Kelley et al. 2018; Mingarelli et al. 2017) despite non-detection in the search for both individual MBH binaries and anisotropy in the NANOGrav 15 yr Data Set (Agazie et al. 2023b,c). From the discrete nature of the GWB spectrum, Agazie et al. (2025) investigated the possibility that a loud MBH binary causes the GWB spectrum to deviate from a power law.

Using the galaxy catalog from the 2 Micron All Sky Survey (2MASS; Skrutskie et al. 2006), together with galaxy merger rates from the cosmological simulation Illustris (Genel et al. 2014; Rodriguez-Gomez et al. 2015), Mingarelli et al. (2017) estimated that there are on average 91 ± 7 detectable CW sources within 225 Mpc over the full sky, and a 20% departure from an isotropic GWB induced by local unresolved sources. The authors pointed out that the best combination of pulsars will boost the number of CWs detections by a fac-

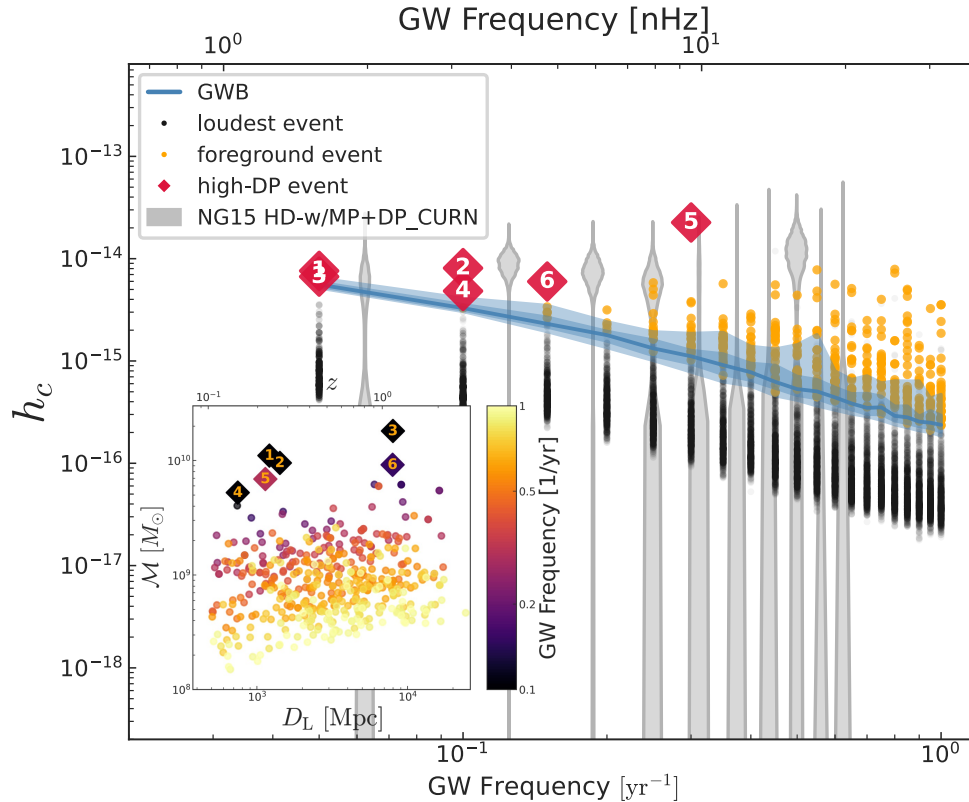


Figure 1. 100 realizations of the low-frequency GW sky based on the mergers in ASTRID. The blue curve represents the median GWB spectra over all realizations, with the inner/outer shaded region corresponding to $1\sigma/2\sigma$ intervals. Black dots plot the loudest event in each realization at each frequency bin. The foreground events, which have higher h_c than the GWB are marked by orange dots. The grey shaded area is the NANOGrav 15Yr GWB. We highlight the events with high detection probability (with $DP > 0.1$) using red diamonds. The insert shows the distribution of the chirp mass \mathcal{M} and the luminosity distance D_L for all foreground sources, color-coded by the observed frequency. The high-DP events, marked by the same index as the GWB plot, are plotted by diamonds.

tor of 4 compared to using the all-sky averaged sensitivity curve, which underlines the importance of pulsar and MBH sky location.

Utilizing the MBH binary population from the Illustris cosmological hydrodynamic simulation, Kelley et al. (2018) calculated the plausible detection prospects for GW single sources and predicted that they are as detectable as the GW background. Gardiner et al. (2024) investigated the detectability of CWs over a wide range of parameter space, including the binary evolution prescription. They predict that the most detectable CW sources are in the lowest frequency bin for a 16.03-yr PTA, having masses from $10^9 \sim 10^{10} M_\odot$ and are ~ 1 Gyr ($z \sim 0.2$) away.

This paper is organized as follows. In Section 2 we introduce the simulation ASTRID and the methods used to simulate single GW events. In Section 3, we present our CW prediction, and provided a detailed analysis of the properties of the high-detectability sources. Finally, we conclude in Section 4.

2. METHODS

In this work, we use the MBH merging population from the ASTRID cosmological hydrodynamic simulation to model the low-frequency GW sky. ASTRID is the largest cosmological hydrodynamical simulation, in terms of particle load, so far run to $z = 0$. It contains 2×5500^3 particles in a box $250h^{-1}\text{Mpc}$ per side, where $h = 0.6774$. Here we briefly introduce the basic parameters and BH modeling for ASTRID, and refer readers to Ni et al. (2022); Bird et al. (2022); Ni et al. (2024) for more details. The mass resolution of ASTRID is $m_{\text{DM}} = 6.74 \times 10^6 h^{-1} M_\odot$ and $m_{\text{gas}} = 1.27 \times 10^6 h^{-1} M_\odot$. The gravitational softening length is $\epsilon_g = 1.5h^{-1}$ kpc for all particles. MBHs are seeded with their mass stochastically drawn from $3 \times 10^4 h^{-1} M_\odot$ to $3 \times 10^5 h^{-1} M_\odot$. The gas accretion rate of black holes is given by the Bondi-Hoyle rate, and super-Eddington accretion is allowed with an upper limit of twice the Eddington accretion rate. With a radiative efficiency $\eta = 0.1$ (Shakura & Sunyaev 1973), the black hole radiates with a bolometric luminosity L_{bol} proportional to the accretion rate: $L_{\text{bol}} = \eta \dot{M}_{\text{BH}} c^2$. Both AGN thermal and kinetic feedback models are included. A subgrid dynamical friction model is used based on the prescription in Tremmel

et al. (2015); Chen et al. (2022) to capture the dynamics of MBHs as they merge. The dynamical friction significantly affects the MBH binary populations and predictions for the GWB (Chen et al. 2025). Two black holes merge when their separation is within $2\epsilon = 3\text{ckpc}/h$ and they are gravitationally bound to the local potential.

To model the GW signals detected in PTA bands, we need to evolve the MBH binaries to sub-parsec scales. In this work, we follow Chen et al. (2025) and use the phenomenological hardening model `HoLodeck`¹. We assume circular orbits for all the binaries. Kelley et al. (2018) evolved the Illustris MBH binaries with varying eccentricity, showing that eccentricity only moderately affects a MBH binary’s detection probability. We use the same parameter settings as Chen et al. (2025), which are based on the best-fit value of the *Phenom+Astro* analysis in Agazie et al. (2023d). Given the evolved population of binaries, the production of GW signals is estimated based on the steps laid out by Sesana et al. (2008). To create discrete realizations of GWB sources from simulation events, we use the method described in Kelley et al. (2017) to weight each MBH binary from ASTRID using a Poisson distribution. We refer the readers to Appendix A and Appendix B in Chen et al. (2025) for more details related to this part.

Given the strain of each source, we calculate the detection probability (DP) and the expected number $\langle N_{\text{SS}} \rangle$ of detected single sources based on the prescription of Rosado et al. (2015). We provide more details in Appendix A.

3. RESULTS

3.1. Characteristic Strain and DP

Drawing on the MBH mergers in ASTRID down to redshift $z = 0.15$, we generate 100 realizations of the low-frequency GW sky covering the frequency range $0.05/\text{yr} < f < 1/\text{yr}$ (i.e., $1.6 \sim 32$ nHz) with a timing cadence $\Delta t = 0.05$ yr. The results are presented in Fig. 1. The blue curve represents the median GWB across all realizations, and the inner/outer shaded region shows the $1\sigma/2\sigma$ intervals. Black dots show the loudest event in each realization at each frequency bin, and orange dots represent the foreground events. In this work, we define the foreground events as those having higher strain h_c than the GWB in the same realization. Due to the low GWB at high frequencies, there are more foreground events at $f \sim 1/\text{yr}$ compared to low frequencies. At low frequencies $f < 0.1/\text{yr}$, all the realizations include loud mergers with $h_c > 10^{-16}$, while only 5 of them are foreground sources. In the insert of Fig. 1, we show the chirp mass \mathcal{M} vs. luminosity distance D_L of all the foreground events, color-coded by frequency. The correlation between \mathcal{M} and D_L is not obvious, except that the lower bound of \mathcal{M} extends to smaller values with

smaller D_L . The expected color gradient in the points is clearly seen, however, showing how low chirp mass events appears in higher frequency bins.

We calculate the DP for all the foreground sources using the prescription described in Appendix A. The results are shown in the top panel in the left column of Fig. 2. Large circles represent the foreground events from 100 realizations, color-coded by h_c . If one merger is observed as a foreground event at the same frequency in different realizations, we only show it once with the highest DP. As a comparison, we also plot the DP for the loudest events in each frequency bin using small black dots.

There are only 6 sources that have DP higher than 0.1. We mark them as “high-DP sources”, and show their positions among the foreground distribution in Fig. 1, 2, 4, and 5. Most of the high-DP sources are among the lowest frequencies. The most likely frequency of detection is predicted by estimating the DP-weighted frequency across all mergers: $\langle f_{\text{fore}} \rangle = \sum_i \text{DP}_i f_i / \sum_i \text{DP}_i = 0.73/\text{yr}$, where DP_i and f_i are the DP and frequency for a specific source. The DP drops rapidly with increasing frequency, and there are no mergers with $\text{DP} > 10^{-6}$ with $f > 0.5/\text{yr}$.

The second panel in the left column of Fig. 2 shows the occurrence rate, i.e., the fraction of the 100 realizations that host at least one foreground event in the specific frequency bin. Due to the relatively low GWB at the high- f end, more mergers can be resolved as CW, leading to higher occurrence rates. The occurrence rate predicted here is generally consistent with Kelley et al. (2018). The lower two panels show the probability of detecting at least one single source at f : $\text{DP}(f)$, and the expected number of the detected single sources N_{SS} . We combine the foreground events from 100 realizations, and the shaded areas represent the 1σ range computed from 500 sets of sky-positions settings (see Appendix A). Although the occurrence rate at the low- f end is very low ($\sim 5\%$ at $f < 1/\text{yr}$) compared to the high f end ($\gtrsim 20\%$ at $f > 1/\text{yr}$), N_{SS} at low- f outweighs that at high- f . This is because all the foreground events at $f \lesssim 1/\text{yr}$ have very high DP, as shown in the top panel of the column. Since the lowest frequency is determined by the observation duration T , increasing T would significantly boost the chance to observe CW sources. The total number of the expected single sources is $\langle N_{\text{SS}} \rangle = 0.12$.

3.2. MBH pair properties

To explore the frequency dependence of the foreground sources, in the left column of Fig. 2 we display the redshifts z (upper panel), masses of merging MBH $M_{\text{tot}} = M_{\text{BH},1} + M_{\text{BH},2}$ (middle panel), and MBH mass ratios $q = M_{\text{BH},2}/M_{\text{BH},1}$ (bottom panel) for all the foreground sources as a function of frequency. $M_{\text{BH},1}$ and $M_{\text{BH},2}$ are the mass of the primary and secondary MBH, respectively. In each panel, blue curves

¹ <https://github.com/nanograv/holodeck>

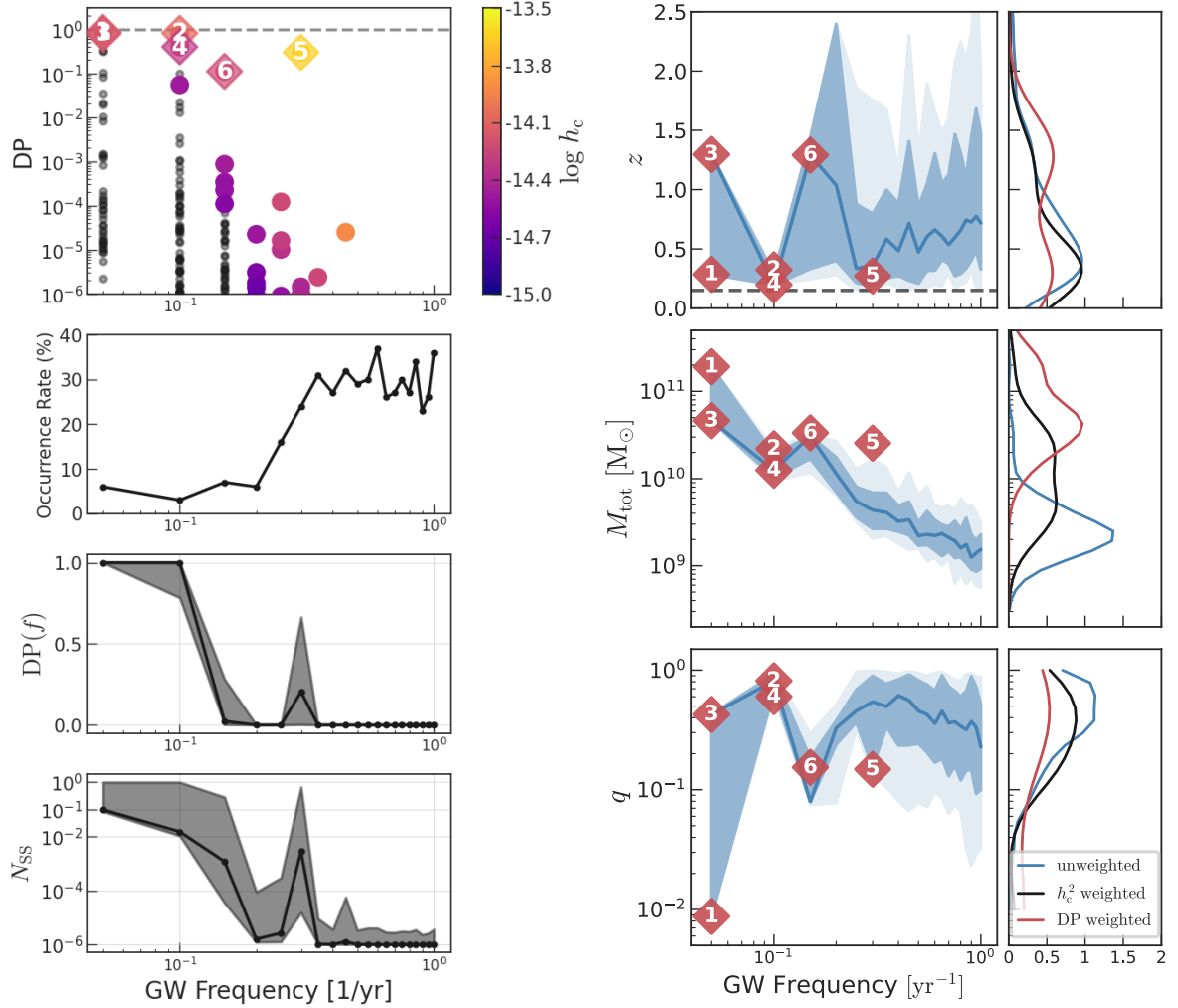


Figure 2. The properties of foreground events over 100 realizations. *Left Column:* the top panel shows the DP values for each foreground event (large circles color-coded by the strain) compared to the 10 loudest events (small black dots). We highlight the sources with DP > 0.1 (high-DP events) by diamonds. The second/ third /fourth panels show the occurrence rate / DP / the expected number of the detected CW sources N_{SS} at a function of frequency. The grey shaded areas are the 1σ region over different sky-position settings (see Appendix A). *Right Column:* From top to bottom, we show the redshift z , the total mass of the merging BHs ($M_{tot} = M_{BH,1} + M_{BH,2}$), and the mass ratio $q = M_{BH,2}/M_{BH,1}$ for all the CW sources at each frequency. In each panel, the median (blue curves), 1σ intervals (dark shaded area), and 2σ intervals (light shaded area) are plotted. In the right frame of each panel, we show the unweighted (blue), h_c^2 -weighted (black), and DP-weighted (red) PDF.

Table 1. The 6 GW sources with DP > 0.1

| | z_{merge} | $\log M_{\text{BH},1} [M_{\odot}]$ | q | $\log \text{SFR} [M_{\odot}/\text{yr}]$ | $\log M_{*,\text{gal}} [M_{\odot}]$ | $\log M_{\text{FOF}} [M_{\odot}]$ |
|----------|--------------------|------------------------------------|------|---|-------------------------------------|-----------------------------------|
| system 1 | 0.3 | 11.3 | 0.01 | 2.8 | 12.6 | 14.8 |
| system 2 | 0.3 | 10.1 | 0.81 | 3.2 | 12.9 | 15.2 |
| system 3 | 1.3 | 10.5 | 0.43 | 3.2 | 12.7 | 14.7 |
| system 4 | 0.2 | 9.9 | 0.60 | 2.6 | 12.3 | 14.6 |
| system 5 | 0.3 | 10.4 | 0.15 | 3.3 | 12.9 | 15.2 |
| system 6 | 1.3 | 10.5 | 0.15 | 3.0 | 12.3 | 14.4 |

show the median value, and the dark (light) shaded areas are the 1σ (2σ) regions.

As we have seen from the insert panel in Fig. 1 merger mass is strongly correlated with frequency. At low frequency, the foreground population is dominated by the massive mergers:

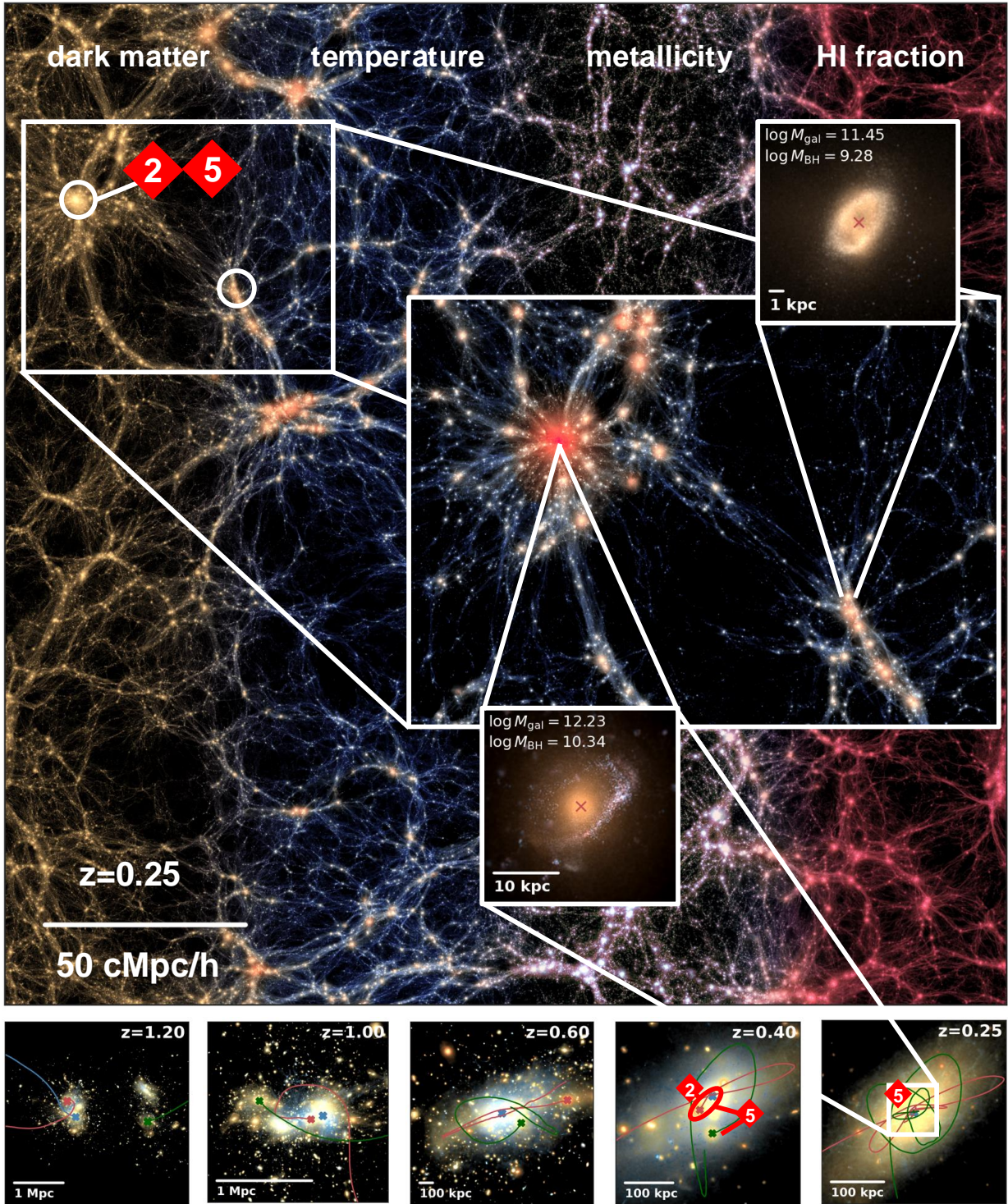


Figure 3. A visualization of the spatial region around the high-DP event system 2 and system 5 at $z = 0.25$. These two systems involve a triple merger in the central galaxy of a massive galaxy cluster. We zoom into a rectangular region around it, which includes another foreground event, and show the gas density field color-coded by temperature (red=hot). Additional small inserts show the grz -band flux of the host galaxies of the two foreground sources, with the merging remnant MBH marked by red crosses. The panels in the bottom row illustrate the orbital evolution of the triple merger in system 2 and 5. In each frame, the blue/red/green crosses mark the position of the primary/secondary/third MBH. Their trajectories are plotted with corresponding colors. The black holes involved in the events that are part of the triple merger (system 2 and then system 5) are indicated in the bottom right two panels. In the frames with $z \leq 1$, the trajectories are plotted relative to the primary MBH. The underlying field is the star density color-coded by the star age, with blue to yellow representing young to old stars.

all the sources observed at $f < 0.1/\text{yr}$ are above $10^{10} M_{\odot}$. However, we see that neither redshift nor mass ratio show any obvious dependence on the observed f .

We plot the one-dimensional probability distribution function (PDF) for z , M_{tot} , and q in the right column of Fig. 2. The blue, black, and red curves represent the unweighted, h_c^c -weighted, and DP-weighted PDF. Examining the PDF of z , we see that a large fraction of the foreground sources occurs below $z < 1$, and the peak for the unweighted PDF is at $z \sim 0.3$ ($D_L \sim 1600$ Mpc). After weighting by the gravitational energy (h_c^2), the peak moves even lower to $z \sim 0.2$. This is expected since low- z sources generally produce higher h_c . The PDF weighted by DP, however, is double-peaked, with peaks at low redshift $z \sim 0.2$ and around $z = 1.2$. The latter peak is caused by the two high-DP events: system 3 and system 6. The drop in the PDF at low z is due to the decreasing MBH merger rate: as discussed in Chen et al. (2025), the merger rate of massive MBHs (with $M_{\text{tot}} \geq 10^9 M_{\odot}$) in ASTRID starts to drop below $z < 0.5$, implying that there are more supermassive mergers to be detected at high redshift rather than in the local Universe ($z \sim 0$). An individual example of such a massive event could change the shape of the DP-weighted z distribution, which highlights that PTA has a large probability of observing mergers with $z > 1$. From the lower right panel of Fig. 2 we can see that most CW sources are major mergers with $q \gtrsim 0.1$, and the median q is around 0.5.

3.3. High-DP CW sources

In this section, we present more details about the 6 high-detectability CW sources with $\text{DP} > 0.1$. In Table 1, we list the properties of the merging MBHs, and the masses of the host galaxy and Friend-Of-Friends (FOF) halo. These 6 sources are all from the high mass end, with the total MBH masses $M_{\text{BH}} > 10^{10} M_{\odot}$. However, they cover a wide range in redshift ($z < 1.3$) and mass ratio ($0.01 \lesssim q \leq 1$). All these sources are located in the massive galaxies with $\log M_{\star, \text{gal}} > 10^{12} M_{\odot}$, and they are all the central galaxies of their halo. This highlights that central cluster galaxies would be a hotspot for detectable CW sources.

Remarkably, among these 6 high-DP sources, System 2 and system 5 are involved in the same triple merger event. System 2 is the first merger, which involves MBHs with masses $1.2 \times 10^{10} M_{\odot}$ and $9.9 \times 10^9 M_{\odot}$ at $z = 0.32$. It is observed at $f = 0.1/\text{yr}$ as a CW source, with $\text{DP}=0.89$. System 5 is the second merger that occurs 480 Myr later, at $z = 0.27$, and involves a $2 \times 10^{10} M_{\odot}$ MBH and a $3 \times 10^9 M_{\odot}$ MBH. It is observed at $f = 0.3/\text{yr}$ with a DP of 0.3.

Figure 3 shows a visualization of the spatial region around this triple merger, marked by red diamonds, at $z = 0.25$. We zoom into a rectangular region around it, which includes another foreground event (the white circle without red dia-

monds), which however has very low DP. We show the gas density field color-coded by temperature (red=hot) in this zoom region. Additional small inserts show the grz -band flux of the host galaxies of the two foreground sources, with the merging remnant MBH marked by red crosses. The host galaxy of the remnant of the triple merger has a stellar mass of $\log M_{\star} = 12.93$, and a total BH mass of $\log M_{\text{BH}} = 11.20$.

The orbital evolution of the triple merger is shown in the lower panels in Fig. 3, starting at $z = 1.2$ and continuing until the end of the triple merger. Following the sequence over this 6 Gyr period, we can see the formation of the most massive galaxy in this cluster. At $z = 1.2$ several distinct galaxies are visible, most of which merge over the next 4 Gyr without the most massive BHs merging. High-DP source 2 occurs in the center of the brightest cluster galaxy (BCG), and then a smaller galaxy containing the last of three MBHs falls into the BCG in an act of galactic cannibalism (e.g., Hsu et al. 2022). This is followed by the final merger, high-DP source 5.

3.4. Dual AGN

In this section, we study the correlation between foreground events and Dual AGN, which has an important implication for future searches for the EM counterpart of GW single sources. We use the same definition of dual AGN as Chen et al. (2023): if the bolometric luminosity of the MBH $L_{\text{bol}} > 10^{43}$ erg/s, the MBH is classified as an AGN. A pair of AGNs is classified as dual AGN if the separation between them is smaller than 30 kpc. To focus on the same mass range as the PTA CW sources, we only study dual AGNs with total M_{BH} larger than $10^8 M_{\odot}$.

In the left panel of Fig. 4, we show the distribution of the bolometric luminosity of the primary MBH ($L_{\text{bol},1}$) vs that of the secondary MBH ($L_{\text{bol},2}$) for the foreground event population. In the upper right, both MBH are bright enough that the event is categorized as coming from a dual AGN. This encompasses the vast majority (88.1%) of the foreground events. All the other CW sources (11.9%) are ‘‘One-AGN pair’’, in which one of the merging MBH is AGN, while the other is not. Hence, all the CW sources in the frequency range $0.05/\text{yr} < f < 1/\text{yr}$ are involved in AGN activity.

We further investigate the dual AGN population in the right panel of Fig. 4. Looking at the luminosity L_{bol} vs MBH mass of dual AGN at $z = 0.3$, we can see that the foreground dual AGN sources (marked by crosses) cover the whole luminosity range, but they preferentially pick out BHs at the high mass end. Of the dual AGN with $M_{\text{tot}} \geq 10^8 M_{\odot}$ at $z = 0.3$, only 0.7% will evolve to become foreground sources. In Fig. 4 insert, we can see that the fraction of dual AGNs that evolve to foregrounds, f_{fore} , doesn’t appear to evolve with redshift and stays at the $\sim 1\%$ level from $0.3 < z < 2.5$.

3.5. Host Galaxies

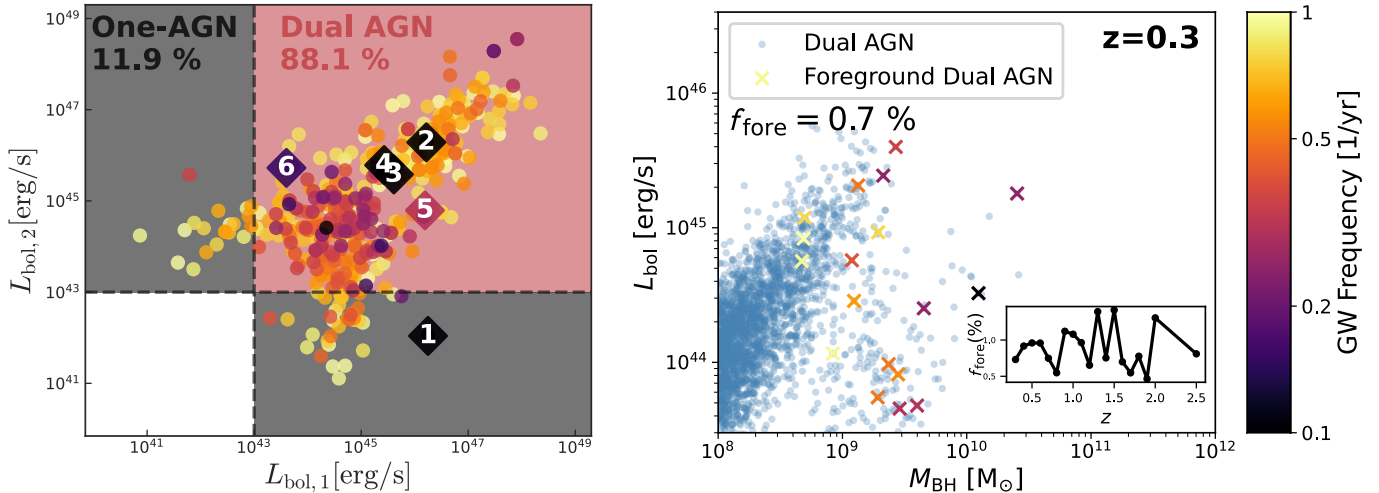


Figure 4. *Left:* The distribution of the bolometric luminosity of the primary MBH ($L_{\text{bol},1}$) and the secondary MBH ($L_{\text{bol},2}$) for the foreground event population. The dots are color coded by the observed frequency. The horizontal and vertical black dashed lines mark the AGN luminosity limit: we define an MBH with $L_{\text{bol}} > 10^{43}$ erg/s as an AGN. The red shaded area on the upper right corner represents the Dual AGN regions, where both MBH in the merging pair are AGNs. Dual AGN comprise 88.1% of the foreground events. The two black shaded areas represent one-AGN regions, for which only one of the MBHs is an AGN, and contain 11.9% of the foreground events. *Right:* The distribution of the bolometric luminosity L_{bol} and the merging MBH mass M_{BH} for the dual AGNs at $z = 0.3$. The blue dots are the whole dual AGN population in ASTRID at the specific redshift. The crosses are the events among the dual AGNs that evolve to be foreground events within 1 Gyr. The crosses are color coded by the observed GW frequency. The two panels share the color bar on the right.

We identify the galaxy hosting the remnant of each CW source in the closest snapshot following the merger. In Fig. 5 we show the $M_{\star} - M_{\text{BH}}$ (left panel) and specific star formation rate ($s\text{SFR}$) versus the galaxy stellar mass (right panel) of the foreground events (colored dots) compared to all the galaxies in ASTRID with $z > 0.2$ (underlying grey distribution). Turning first to the $M_{\star} - M_{\text{BH}}$ relation, we can see that the foreground sources follow a trend consistent with that of the whole galaxy population. The median relation for foregrounds closely tracks the relation for all galaxies across the whole $M_{\star,\text{gal}}$ range. The individual high-DP sources do not appear to differ significantly from the mean relation, except for source 1, which appears to be an overmassive MBH. The events arising from a triple merger (system 2 and system 5) are associated with the most massive end of the relation.

The 6 high-DP sources all have a $s\text{SFR}$ above $10^{-10}/\text{yr}$. Considering their huge mass, these galaxies are undergoing significant star formation. In Table 1, we list the total SFR for each, and see that these galaxies all have a SFR larger than $100 M_{\odot}/\text{yr}$, showing no signature of quenching. This is likely due to the recent galaxy merger activity which preceded the GW event. In the galaxy plot for the triple merger in Fig. 3, shows obvious signs of disturbances (tidal streams, shells).

4. DISCUSSION AND CONCLUSIONS

This work, using the ASTRID cosmological hydrodynamic simulation, provides significant new insights into the nature of detectable (in ~ 20 yr) CW sources for PTAs. Our anal-

ysis, focusing on supermassive black hole (SMBH) mergers, reveals several crucial findings:

- *Central Cluster Galaxies as a Hotspot:* We find that the most detectable CW signals are produced by SMBH mergers with masses exceeding $10^{10} M_{\odot}$, predominantly located within the massive central galaxies of galaxy clusters. This highlights a previously under-appreciated connection between these high-mass mergers and the formation process of central cluster galaxies.

- *Remarkable Sequential Mergers:* A particularly striking result from the ASTRID simulation is the identification of two high-detection-probability CW events arising from two subsequent mergers within the same cluster core, predicted at frequencies of 2 and 10 nanohertz. This triple merger scenario, found within the simulation, represents a novel and potentially highly observable event for PTAs.

- *High-Detection Probability Sources:* Our analysis indicates that (at the current 16.8 yrs of PTA observations) only a small fraction of simulated mergers have a high detection probability ($\text{DP} > 0.1$), with only 6 sources exhibiting a high DP. These high-DP events, including the sequential mergers, are typically associated with the highest-mass systems.

- *Redshift Distribution:* The redshift distribution of all foreground sources is quite spread out, with a peak at $z \sim 0.2$, and minor peak at $z \sim 1.2$ (at lower significance as it is due to only two high-DP systems). When weighted by gravitational wave energy, a single peak emerges at $z \sim 0.2$.

- *SMBH Merger Properties:* Most foreground sources are major mergers with mass ratios of $q > 0.1$ and a median q of

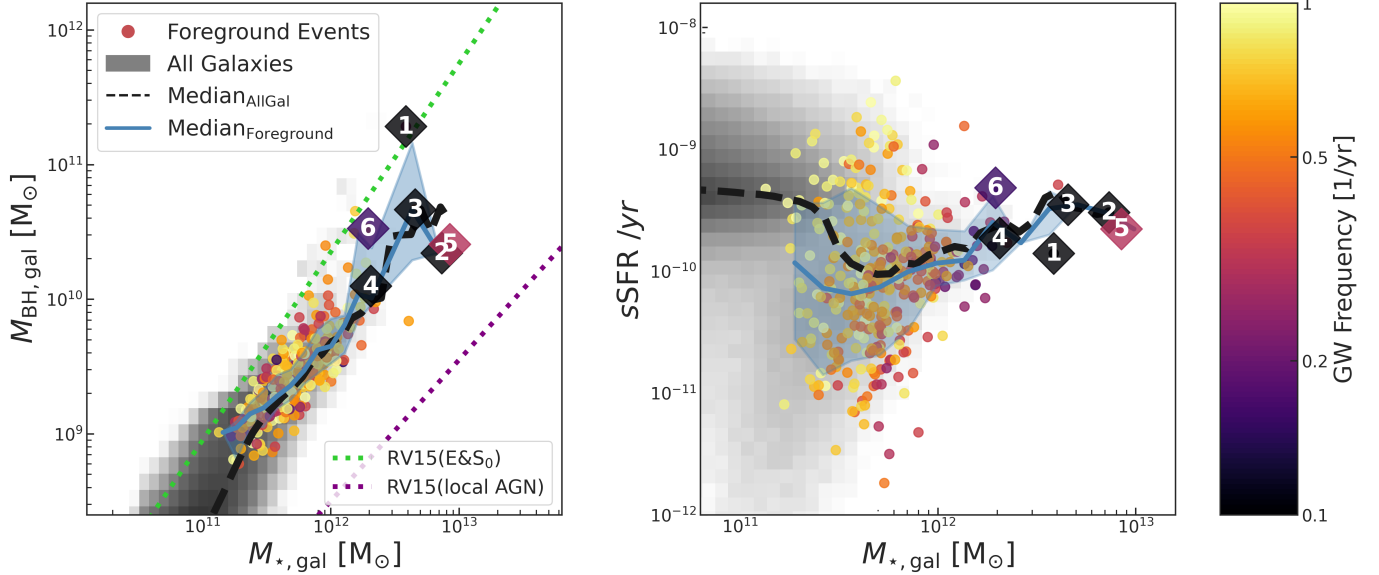


Figure 5. The host galaxy properties of the foreground events (colored dots) compared to all the galaxies in ASTRID (grey pixels). The underlying darker regions represent higher number density. The dots in two panels share the same colorbar, which is shown in the right. *Left:* the distribution of the stellar mass and the black hole mass in the galaxies. *Right:* the distribution of the specific star formation rate $sSFR$ versus the stellar mass in the galaxies. The black dash/blue solid curves show the median values for all galaxies/foreground sources.

around 0.5. The total mass of these mergers is typically high, with almost no events with chirp masses below $\sim 10^9 M_\odot$ likely detectable.

- *Link to (Dual) AGN:* We find a strong association between foreground events and AGN activity. The majority (88.1%) of foreground events are associated with dual AGN, where both black holes in the merging pair are active. However, only a small fraction (0.7%) of dual AGN at $z = 0.3$ evolve into foreground sources.

- *Host Galaxy Properties:* The host galaxies of these foreground events are generally massive, with stellar masses typically exceeding $10^{12} M_\odot$. There’s a suggestion that galaxies at the lower end of the stellar mass range tend to be more quenched, compared to the foreground events, which are associated with the formation of the central cluster galaxy.

- *Implications for PTA Observations.* The relatively low number of expected single sources, with an expected total number of $\langle N_{SS} \rangle = 0.12$ reinforces the importance of considering both the GWB and individual CW sources when interpreting PTA data.

Given our results, what guidance can we offer in searches for the EM counterparts of individual PTA sources? We have seen that in ASTRID the sources are in massive galaxies, with the most prominent being host to two events lying at the center of a galaxy cluster of mass $10^{15} M_\odot$ at $z = 0.25$. Such objects have highly biased clustering (e.g., [Desjacques et al. 2018](#), [De Lucia & Blaizot 2007](#)), leading to an expected anisotropy in the GWB. Whether they can be localized in the future depends on the SNR. As an example, [Truant et al. \(2024\)](#) model the detectability of individual events with idealized MeerKAT

and SKA experiments, finding that binaries detected at $5 < \text{SNR} < 10$ have a median sky-localization area of $\Delta\Omega \sim 200 \text{ deg}^2$ (falling to $\sim 10 \text{ deg}^2$ for $\text{SNR} > 15$). As these authors state, this error ellipse of $\sim 1 - 10 \text{ deg}$ radius makes localization challenging. On the other hand, the number of galaxy clusters with mass $\geq 10^{15} M_\odot$ and $z < 0.25$ is less than 100 ([Abell 1958](#); [Reiprich & Böhringer 2002](#); [Böhringer et al. 2017](#)). This leads to a mean angular separation of $> 20 \text{ deg}$ and consequently a low chance of confusion.

In ASTRID the triple merger occurs in a BCG. This and several other GW events take place in systems that are not “dry” mergers; these galaxies exhibit substantial star formation rates, on the order of hundreds of solar masses per year. Star-forming populations of BCGs have been observed at these moderate redshifts, for example, in the KIDS survey [Castignani et al. \(2022\)](#). While the presence of dual AGN appears to be a necessary condition for a merger to become a foreground GW event, it is not sufficient. We find that fewer than 1% of dual AGN systems evolve into high-DP events. The ideal source seems to be a galaxy at the center of a cluster that has undergone recent (or still ongoing) mergers—either through the merger of at least two large galaxies or cannibalism of a smaller galaxy by a larger elliptical. A key detail is that all systems we have found retain enough residual gas to fuel a high total star formation rate. This is another factor that could enhance the detectability of the associated CW signal.

Our study validates the theoretical framework by showing similarities to other simulation based works and observational constraints. These results reinforce the idea that single source detections, in addition to the GWB, are likely, and important

for probing the population and evolution of SMBHBs. The possible detection of CWs in current/upcoming data, combined with the growing understanding of GWB, further refines our understanding of the parameter space. This research underscores the importance of considering foreground sources

when interpreting PTA data, and helps to guide future multi-messenger searches for the electromagnetic counterparts of these events. Future work should focus on improving the modeling of binary evolution and the inclusion of more realistic noise models, and exploration of the degeneracies between model parameters, to better constrain theoretical predictions.

APPENDIX

A. DETECTION PROBABILITY

We calculate the detection statistics (DP) following the prescription provided in [Rosado et al. \(2015\)](#). We include 68 pulsars with the 16.03 yr duration, consistent with [Agazie et al. \(2023a\)](#). The position of pulsars and single sources are randomly generated, and uniformly distributed across the sky. For the noise spectral density of pulsars, we include both white noise and red noise:

$$S = 2\Delta t \sigma_{\text{WN}}^2 + \frac{h_{\text{rest}}^2}{12\pi^2 f^3}, \quad (\text{A1})$$

where the term $2\Delta t \sigma_{\text{WN}}^2$ is the contribution from the white noise. Δt is the observing time cadence, which is set to be $\Delta t = 0.05$ yr in this work. We set the whose noise root-mean-square $\sigma_{\text{WN}} = 3 \mu\text{s}$, which is consistent with the model d used in [Kelley et al. \(2018\)](#). For the red noise term, h_{rest} is the sum of characteristic strain from all the other single sources as well as the GWB at this frequency:

$$h_{\text{rest},j}^2 = h_{\text{c,BG}}^2 + \sum_{i \neq j} h_{\text{c,SS},i}^2. \quad (\text{A2})$$

With the noise model, we then calculated the DP for each single source (DP_j). The probability of detecting any of a single source is

$$\text{DP}_{\text{SS}} = 1 - \prod_j [1 - \text{DP}_{\text{SS},j}]. \quad (\text{A3})$$

The expected number of detected sources at frequency f is $\langle N_{\text{SS}} \rangle_f = \sum_j \text{DP}_{\text{SS},f,j}$, where $\text{DP}_{\text{SS},f,j}$ is the DP of a single source with the index of j at the frequency f . As pointed out in [Mingarelli et al. \(2017\)](#), the relative position between single sources and the pulsars on the sky has a significant influence on the resultant N_{SS} . To account for the effect of observed sky-position, we generated 500 sets of parameters related to observation (rather than the GW intrinsic properties). This is the so-called ‘sky realization’ in [Gardiner et al. \(2024\)](#). Each set includes randomly assigned pulsar position, single source position, inclination, polarization and the GW phase. The DP for a CW source that occurred in a specific strain realization is the DP value averaged over 500 observation sets.

REFERENCES

- Abell, G. O. 1958, *ApJS*, 3, 211, doi: [10.1086/190036](https://doi.org/10.1086/190036)
- Agazie, G., Anumarlapudi, A., Archibald, A. M., et al. 2023a, *ApJL*, 951, L8, doi: [10.3847/2041-8213/acdac6](https://doi.org/10.3847/2041-8213/acdac6)
- . 2023b, *ApJL*, 951, L50, doi: [10.3847/2041-8213/ace18a](https://doi.org/10.3847/2041-8213/ace18a)
- . 2023c, *ApJL*, 956, L3, doi: [10.3847/2041-8213/acf4fd](https://doi.org/10.3847/2041-8213/acf4fd)
- . 2023d, *ApJL*, 952, L37, doi: [10.3847/2041-8213/ace18b](https://doi.org/10.3847/2041-8213/ace18b)
- Agazie, G., Antoniadis, J., Anumarlapudi, A., et al. 2024, *ApJ*, 966, 105, doi: [10.3847/1538-4357/ad36be](https://doi.org/10.3847/1538-4357/ad36be)
- Agazie, G., Anumarlapudi, A., Archibald, A. M., et al. 2025, *ApJ*, 978, 31, doi: [10.3847/1538-4357/ad93d5](https://doi.org/10.3847/1538-4357/ad93d5)
- Bird, S., Ni, Y., Di Matteo, T., et al. 2022, *MNRAS*, 512, 3703, doi: [10.1093/mnras/stac648](https://doi.org/10.1093/mnras/stac648)
- Böhringer, H., Chon, G., & Fukugita, M. 2017, *A&A*, 608, A65, doi: [10.1051/0004-6361/201731205](https://doi.org/10.1051/0004-6361/201731205)
- Castignani, G., Radovich, M., Combes, F., et al. 2022, *A&A*, 667, A52, doi: [10.1051/0004-6361/202243689](https://doi.org/10.1051/0004-6361/202243689)
- Chen, N., DiMatteo, T., & Zhou, Y. 2025, *ApJ*, <https://arxiv.org/abs/1302.4485>
- Chen, N., Ni, Y., Tremmel, M., et al. 2022, *MNRAS*, 510, 531, doi: [10.1093/mnras/stab3411](https://doi.org/10.1093/mnras/stab3411)
- Chen, N., Di Matteo, T., Ni, Y., et al. 2023, *MNRAS*, 522, 1895, doi: [10.1093/mnras/stad834](https://doi.org/10.1093/mnras/stad834)
- De Lucia, G., & Blaizot, J. 2007, *MNRAS*, 375, 2, doi: [10.1111/j.1365-2966.2006.11287.x](https://doi.org/10.1111/j.1365-2966.2006.11287.x)

- Desjacques, V., Jeong, D., & Schmidt, F. 2018, *PhR*, 733, 1, doi: [10.1016/j.physrep.2017.12.002](https://doi.org/10.1016/j.physrep.2017.12.002)
- EPTA Collaboration, InPTA Collaboration, Antoniadis, J., et al. 2023, *A&A*, 678, A50, doi: [10.1051/0004-6361/202346844](https://doi.org/10.1051/0004-6361/202346844)
- Gardiner, E. C., Kelley, L. Z., Lemke, A.-M., & Mitridate, A. 2024, *ApJ*, 965, 164, doi: [10.3847/1538-4357/ad2be8](https://doi.org/10.3847/1538-4357/ad2be8)
- Genel, S., Vogelsberger, M., Springel, V., et al. 2014, *MNRAS*, 445, 175, doi: [10.1093/mnras/stu1654](https://doi.org/10.1093/mnras/stu1654)
- Hsu, Y.-H., Lin, Y.-T., Huang, S., et al. 2022, *ApJ*, 933, 61, doi: [10.3847/1538-4357/ac6d66](https://doi.org/10.3847/1538-4357/ac6d66)
- Izquierdo-Villalba, D., Sesana, A., Bonoli, S., & Colpi, M. 2022, *MNRAS*, 509, 3488, doi: [10.1093/mnras/stab3239](https://doi.org/10.1093/mnras/stab3239)
- Kelley, L. Z., Blecha, L., & Hernquist, L. 2017, *MNRAS*, 464, 3131, doi: [10.1093/mnras/stw2452](https://doi.org/10.1093/mnras/stw2452)
- Kelley, L. Z., Blecha, L., Hernquist, L., Sesana, A., & Taylor, S. R. 2018, *MNRAS*, 477, 964, doi: [10.1093/mnras/sty689](https://doi.org/10.1093/mnras/sty689)
- Mingarelli, C. M. F., Lazio, T. J. W., Sesana, A., et al. 2017, *Nature Astronomy*, 1, 886, doi: [10.1038/s41550-017-0299-6](https://doi.org/10.1038/s41550-017-0299-6)
- Ni, Y., Chen, N., Zhou, Y., et al. 2024, arXiv e-prints, arXiv:2409.10666, doi: [10.48550/arXiv.2409.10666](https://doi.org/10.48550/arXiv.2409.10666)
- Ni, Y., Di Matteo, T., Bird, S., et al. 2022, *MNRAS*, 513, 670, doi: [10.1093/mnras/stac351](https://doi.org/10.1093/mnras/stac351)
- Ravi, V., Wyithe, J. S. B., Hobbs, G., et al. 2012, *ApJ*, 761, 84, doi: [10.1088/0004-637X/761/2/84](https://doi.org/10.1088/0004-637X/761/2/84)
- Reardon, D. J., Zic, A., Shannon, R. M., et al. 2023, *ApJL*, 951, L6, doi: [10.3847/2041-8213/acdd02](https://doi.org/10.3847/2041-8213/acdd02)
- Reiprich, T. H., & Böhringer, H. 2002, *ApJ*, 567, 716, doi: [10.1086/338753](https://doi.org/10.1086/338753)
- Rodriguez-Gomez, V., Genel, S., Vogelsberger, M., et al. 2015, *MNRAS*, 449, 49, doi: [10.1093/mnras/stv264](https://doi.org/10.1093/mnras/stv264)
- Rosado, P. A., Sesana, A., & Gair, J. 2015, *MNRAS*, 451, 2417, doi: [10.1093/mnras/stv1098](https://doi.org/10.1093/mnras/stv1098)
- Sato-Polito, G., & Zaldarriaga, M. 2024, arXiv e-prints, arXiv:2406.17010, doi: [10.48550/arXiv.2406.17010](https://doi.org/10.48550/arXiv.2406.17010)
- Sato-Polito, G., Zaldarriaga, M., & Quataert, E. 2024, *PhRvD*, 110, 063020, doi: [10.1103/PhysRevD.110.063020](https://doi.org/10.1103/PhysRevD.110.063020)
- Sesana, A., Vecchio, A., & Colacino, C. N. 2008, *MNRAS*, 390, 192, doi: [10.1111/j.1365-2966.2008.13682.x](https://doi.org/10.1111/j.1365-2966.2008.13682.x)
- Shakura, N. I., & Sunyaev, R. A. 1973, *A&A*, 24, 337
- Skrutskie, M. F., Cutri, R. M., Stiening, R., et al. 2006, *AJ*, 131, 1163, doi: [10.1086/498708](https://doi.org/10.1086/498708)
- Tremmel, M., Governato, F., Volonteri, M., & Quinn, T. R. 2015, *MNRAS*, 451, 1868, doi: [10.1093/mnras/stv1060](https://doi.org/10.1093/mnras/stv1060)
- Truant, R. J., Izquierdo-Villalba, D., Sesana, A., Mohiuddin Shaifullah, G., & Bonetti, M. 2024, arXiv e-prints, arXiv:2407.12078, doi: [10.48550/arXiv.2407.12078](https://doi.org/10.48550/arXiv.2407.12078)
- Xu, H., Chen, S., Guo, Y., et al. 2023, *Research in Astronomy and Astrophysics*, 23, 075024, doi: [10.1088/1674-4527/acdfa5](https://doi.org/10.1088/1674-4527/acdfa5)